nature communications

Article

https://doi.org/10.1038/s41467-026-73523-0

Mitochondrial flagella-like extensions (MitoFLARE) dysfunction triggers STING-mediated immune dysregulation in sepsis

Received: 3 April 2025

Accepted: 25 April 2026

Published online: 25 May 2026

Check for updates

Weilong Hong[1,10], Ruiyan Ma[2,10], Shiyun Long[1,10], Rui Song[1,10], Shuang Ren[1], Xiaoping Ran[1], Junfang Wan[1], Yifei Liu[1], Xiaofeng Li[1], Qian Chen[3], Daqing Ma[3,4], Zhaocai Zhang[5], He Huang[1], Milad Ashrafizadeh[6], João Conde[1,9] ✉, Liangming Liu[7] ✉ & Chenyang Duan[1,8] ✉

Sepsis is an immune dysregulation syndrome triggered by infection, characterized by host self-damage due to immune imbalances. This study focuses on dynamic changes of mitochondrial symbiotic function in host cells during sepsis and systematically investigates dysregulation of mitochondrial communication modes and the intrinsic link between mitochondrial DNA (mtDNA) release and immune dysregulation. We demonstrate that during early-stage LPS treatment, mitochondria actively remodel by extruding flagella-like extensions (termed mitoFLARE). These structures, nanotubes mediating long-distance transport, form through glycosylated TRAK1 binding FHL2 to drive actin network formation, thereby shifting mitochondrial communication from direct fusion to nanotube-mediated transport. This helps maintain dynamic exchange within the inner mitochondrial membrane under LPS treatment. However, as inflammation progresses, deteriorated mitochondrial quality control disrupts the MICOS-SAM complex, abrogates inner-outer membrane anchoring, and suppresses mitoFLARE functions. All these ultimately enhance endoplasmic reticulum-mitochondrial contacts to promote outer membrane rupture and result in mtDNA release into the cytoplasm to activate cGAS-STING signaling, further triggering immune dysregulation and inflammatory storm, culminating in programmed cell death and organ dysfunction. This study elucidates the pivotal role of dysregulated mitochondrial-host symbiosis in sepsis progression and provides important insights into the underlying mechanisms of sepsis-associated immune imbalances, laying a theoretical foundation for targeted therapy development.

Sepsis remains one of the leading causes of death worldwide[1,2] and, indeed, it causes more than 11 million deaths worldwide each year, with an in-hospital mortality rate of 30%–50%, making it one of the most clinical challenges in critical care medicine[3,4]. Despite great efforts made, including the Surviving Sepsis Campaign, the mortality of sepsis has not been significantly improved over the last two decades, indicating that there is an urgent need to explore underlying complex mechanisms[5]. Traditionally, it has been considered that the core trigger of sepsis and subsequent organ damage were directly due to pathogenic damage. However, a paradigm shift occurred with the Sepsis-3.0 definition in 2016, which emphasised organ dysfunction caused by dysregulated host immune responses to be an essential

A full list of affiliations appears at the end of the paper. ✉e-mail: joao.conde@nms.unl.pt; lmliu62@tmmu.edu.cn; duanchenyang1991@cqmu.edu.cn

pathological hallmark of sepsis[6]. This immune dysregulation involves a dynamic immune-imbalance between the cytokine storm and compensatory anti-inflammatory response syndrome, ultimately leading to mitochondrial dysfunction and pyroptosis in initiating multi-level pathological cascades[7].

As the "energy hub" and "signalling integration platform" of eukaryotic cells, mitochondria play a critical role in sepsis pathogenesis. According to the endosymbiotic theory, mitochondria originate from a symbiotic event between α-proteobacteria and Archaea, retaining an independent genome (mitochondrial DNA: mtDNA) and a unique membrane structure throughout evolution[8–10]. This evolutionary legacy endows mitochondria with dual functions, specifically generating more than 90% of the cellular ATP through oxidative phosphorylation and regulating innate immunity via the release of signalling molecules, such as mtDNA and reactive oxygen species (ROS)[11,12]. These may suggest that the core pathogenesis of sepsis is not only caused by direct infection but also driven by dysregulated host immune responses and self-inflicted damage. Immune dysregulation typically involves the overamplification of inflammatory responses, ultimately compromising cellular homeostasis and organ function. However, the underlying mechanisms of immune dysregulation in sepsis remain unclear.

Under physiological condition, mitochondria maintain cellular homeostasis and metabolic balance through inner membrane matrix exchange, and their quality control is achieved via continuous inner membrane fusion (mediated by MFN1/2 and OPA1) and outer membrane fission, mainly regulated by DRP1 to establish a "dynamic equilibrium" that facilitates the clearance of damaged mitochondria and ensures metabolic adaptability[13–15]. Notably, mitochondria not only function alone but also form an intricate symbiotic regulatory system within host cells through dynamic network behaviours, such as fusion/fission balance and mitophagy to maintain endosymbiotic homeostasis[16–18]. As a unique endosymbiotic system, mitochondria not only possess independent genetic material (mtDNA) but also maintain close communication with host cells through dynamic interactions. Recent studies have described mitochondrial nanotunneling as thin double-membrane protrusions that connect spatially separated mitochondria, typically 40–200 nm in diameter and up to 30 μm in length, enabling long-distance exchange of mitochondrial contents and functional complementation under stress conditions[19–21]. However, several critical aspects of mitochondrial nanotunneling remain unresolved. It is unclear how these structures are initiated and dynamically regulated under inflammatory stress, whether the inner and outer mitochondrial membranes play distinct roles during their formation and function, and how their structural transitions are linked to downstream biological consequences, particularly in the context of immune activation.

Emerging evidence suggests that mitochondrial dysfunction contributes to immune dysregulation through mechanisms, such as mtDNA release, cGAS-STING pathway activation, and type I interferon responses; impaired mitophagy leading damage-associated molecular patterns (DAMPs); ROS facilitating NLRP3 inflammasome assembly and driving IL-1β and IL-18 release[22–24]. Recent findings indicate that impaired mitochondrial fusion function is closely associated with a decline in cardiac contractility, suggesting it may play an important role in the pathogenesis of cardiomyopathy. This decline in mitochondrial fusion activity rapidly occurs during in vitro culture of cardiomyocytes, a process mediated by weakened calcium oscillations/contractile activity and reduced expression of mitofusin 1 (Mfn1)[25]. Furthermore, mechanisms of mitochondrial dynamics have been identified, including KIF5B-driven mitochondrial dynamic tubulation, which actively transports nucleoids and facilitates network formation through endoplasmic reticulum-mitochondria contact sites in an Miro1- and MICOS-dependent manner[26,27]. This process is particularly important for nucleoid distribution in the cell periphery and reveals that mitochondrial networks are zonally organized and constructed via distinct mechanisms[28].

Although these studies highlight the critical role of mitochondria in immune dysregulation, the dynamic changes in the mitochondria–host cell endosymbiotic liaison during sepsis and underlying mechanisms remain unclear. Thus, the transformation and dysfunction of mitochondrial communication modes and their intrinsic association with immune dysregulation require further investigation.

In this study, we have addressed the limitations of previous studies by elucidating several key questions regarding the regulatory mechanisms underlying mitochondrial nanotunneling. We determined that the formation of these structures involves distinct stages, including initiation, elongation, and dissolution. We demonstrated that this process is orchestrated by the remodeling of the microtubule and actin cytoskeleton, as well as endoplasmic reticulum–mitochondria interactions. Furthermore, the progressive structural disruption of these nanotunnels leads to mitochondrial membrane rupture, the release of mitochondrial DNA, and subsequent activation of innate immune signaling. Based on these features, we term this mitochondrial nanotunneling, which is physiologically present but robustly induced by stress, as "mitoFLARE," reflecting its dynamic behavior and functional consequences in inflammation, including sepsis.

Mitochondria endosymbiotic function in host cells transiting from active adaptation to dysregulation during sepsis progression

Under physiological condition, mitochondria exhibit highly dynamic behaviour within host cells. They undergo rapid bidirectional movement and transient outer membrane fusion, creating an isolated environment for mitochondrial inner membrane matrix exchange[29]. This ensures the efficient transmission of mtDNA and other essential materials without interference with host cells, as we consistently detected in HL-1 murine cardiomyocytes using Tom20 for outer mitochondrial membrane (OMM) and PKmito for inner membrane (IMM) labelling. (Fig. 1A and Video 1, 2). However, as LPS treatment, mitochondrial motility was decreased, shifting from long-range rapid movements to short-range oscillations (Fig. 1B and Video 3–5). This transition promoted the formation of long-distance, flagellum-like membrane extensions between mitochondria (termed mitoFLARE, structurally corresponding to previously reported nanotunneling; Fig. 1C and Video 6, 7). These dynamic structures can establish physical connections and facilitate content transfer, representing a stress–responsive mode of intermitochondrial communication upon mild LPS treatment.

With the mitoFLARE communication mode, mitochondria extended "long filopodia" composed of both the outer and inner membranes to capture distant mitochondria and facilitate inner membrane matrix exchange (Fig. 1D and Video 8). This phenomenon was also seen in the animal model of sepsis. A significant increase in mitoFLARE structures was observed in the CLP group compared to the control group. These structures were predominantly found in the CLP hearts, and the difference was statistically significant ($p < 0.05$). (Fig. 1E and Supplementary Fig. 1A). Although mitoFLAREs shared similarities with direct fusion, both required outer membrane fusion to establish an isolated environment; the key distinction was the associated mechanisms; direct fusion was determined to rely on transient outer membrane contact for material transfer, whereas nanotube-mediated communication involved in the active extension of mitochondria to form nanotubes. Upon contact with the outer membrane, the materials were transported through the inner membrane along the nanotubes over long distances (Fig. 1A–C). This transition represents a proactive mitochondrial adaptation to LPS treatment, ensuring efficient matrix exchange, while avoiding host cell self-recognition per se.

https://doi.org/10.1038/s41467-026-73523-0

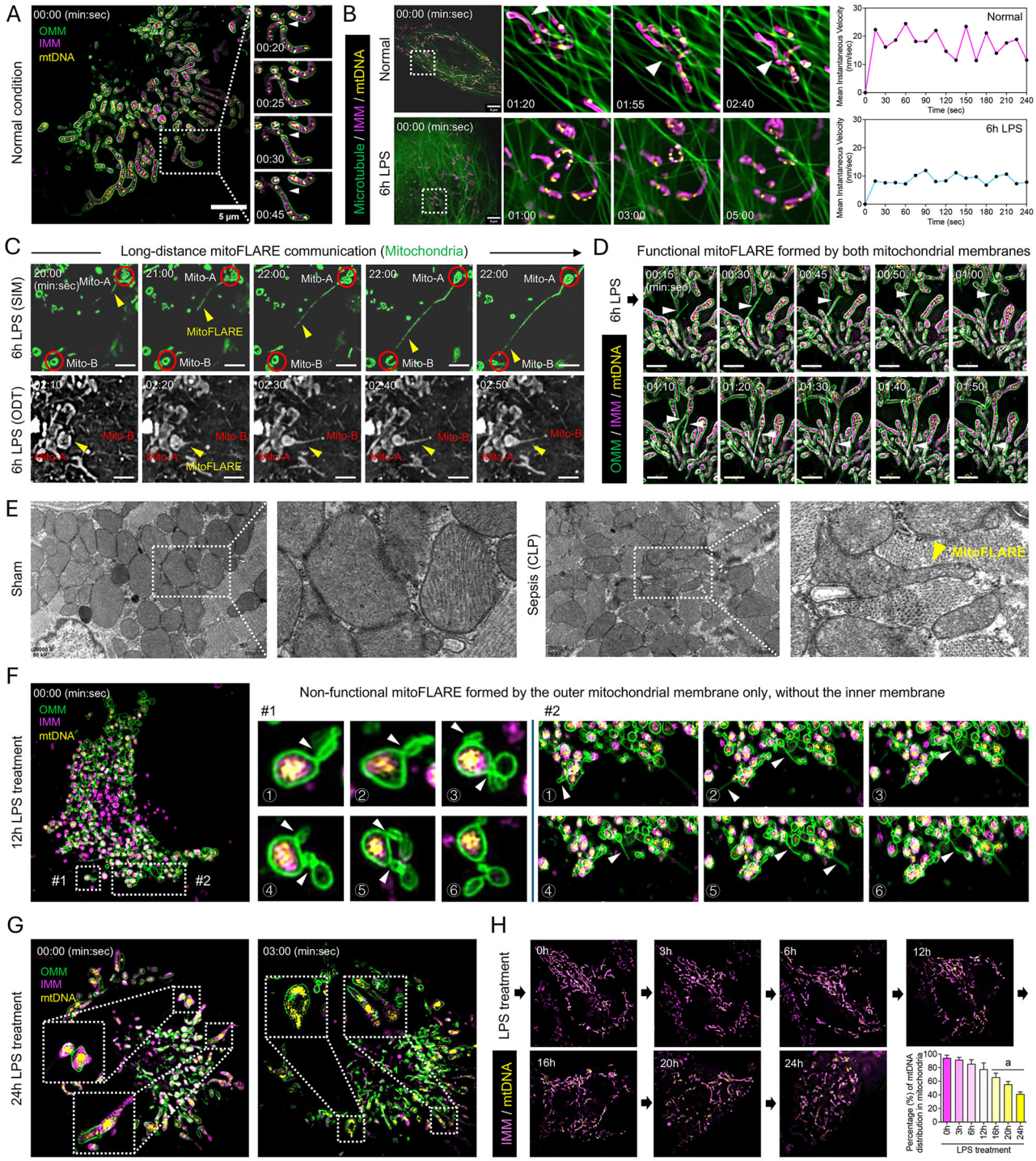

Fig. 1 | The endosymbiosis between mitochondria and host cells has undergone a process from active adaptation to dysregulation in lipopolysaccharide (LPS)-treated HL-1 cells. A HL-1 cells labelled for PK Mito (mitochondrial inner membrane marker, magenta), Tom20 (mitochondrial outer membrane marker, green), and SYBR™ Gold (mitochondrial DNA [mtDNA] marker, yellow). Images of cells were obtained using a multi-SIM (High Sensitivity Structured Illumination Microscope) (bar, 5 μm). **B** HL-1 cells labelled for PK Mito (mitochondrial inner membrane marker, magenta), tubulin (microtubule marker, green), and SYBR™ Gold (mtDNA marker, yellow). Images of cells were obtained using a Multi-SIM (bar, 5 μm). Mean instantaneous velocities of mitochondria in selected ROIs were determined in the normal and 6 h LPS group using HIS-SIM ($n \geq 3$ independent experiments). **C** Time-lapse recording after LPS 20 μg/mL continuous treatment in HL-1 cells for 6 h using a SIM and Nanolive optical diffraction tomography (ODT). Nanolive ODT and SIM recorded mitochondria (green) (bar, 2 μm). **D** HL-1 cells labelled for PK Mito (mitochondrial inner membrane marker, magenta), Tom20 (mitochondrial outer membrane marker, green), and SYBR™ Gold (mtDNA marker, yellow). Images of cells were obtained using HIS-SIM (bar, 2 μm). **E** Distinctive mitochondrial morphological changes were detected via transmission electron microscopy (TEM; 20,000× magnification) in a mouse heart processed with CLP (means ± SD, $n = 3$ biologically independent samples). **F,G** HL-1 cells labelled for PK Mito (mitochondrial inner membrane marker, magenta), Tom20 (mitochondrial outer membrane marker, green), and SYBR™ Gold (mtDNA marker, yellow). Continuous LPS 20 μg/mL treatment in HL-1 cells for 12 h (F) and 24 h (G). Images of cells were obtained using an HIS-SIM (bar, 5 μm). **H** Time-lapse recording of LPS continuous processing in HL-1 cells for 24 h using an HIS-SIM. HL-1 cells were labelled for PK Mito (mitochondrial inner membrane marker, magenta) and SYBR™ Gold (mtDNA marker, yellow) (means ± SD, $n = 3$ biologically independent samples). a: $p < 0.05$ compared with the normal group.

https://doi.org/10.1038/s41467-026-73523-0

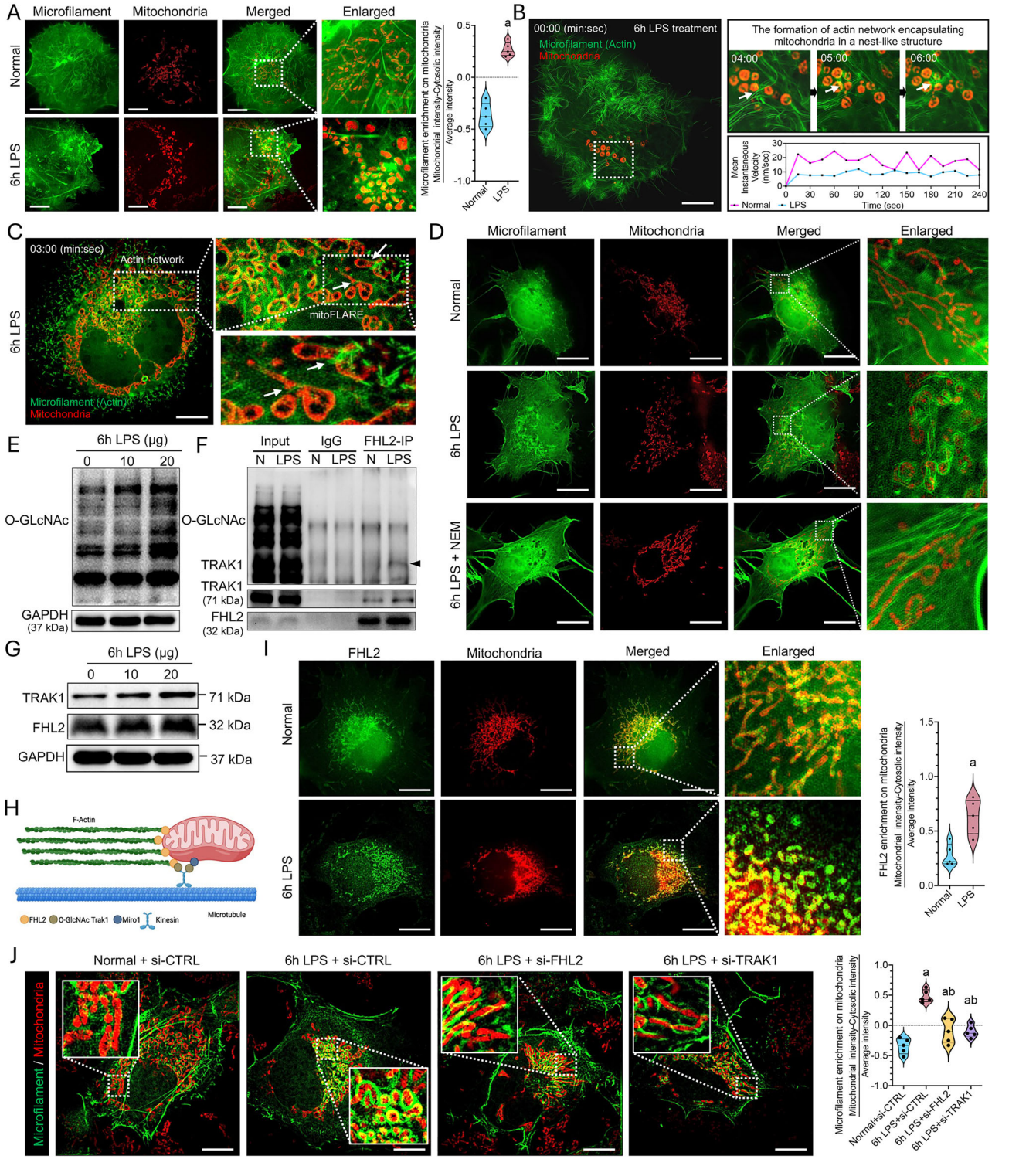

However, as the LPS treatment intensified, mitoFLARE communication gradually failed. Initially, the "long filopodia" were composed of both outer and inner membranes, but with progressive damage, the inner membrane extension capacity weakened, leaving only the outer membrane filopodia intact. This disruption blocked inner membrane matrix exchange, leading to mitochondrial dysfunction (Fig. 1F and Video 9). As the damage intensified, these outer membrane filopodia were eventually ruptured, destroying the isolated environment and causing mitochondrial inner membrane matrix components, such as mtDNA, leaking into the host cell cytoplasm (Fig. 1G and Video 10). This shift signified a transition from active adaptation to endosymbiotic dysregulation, ultimately leading to matrix leakage and host cell damage (Fig. 1H and Video 11). These may indicate that during sepsis onset and progression, the mitochondria–host cell endosymbiotic relationship shifts from active adaptation to dysregulation phase.

Glycosylated TRAK1 induce a transition in the mitochondrial communication mode during active adaptation

To investigate the mechanisms underlying the mitochondrial communication transition under LPS treatment, we labelled the cytoskeletons of live cells. Upon lipopolysaccharide (LPS) stimulation, a dense

Fig. 2 | Glycosylated TRAK1 binds to FHL2 in host cells and drives the formation of actin networks around mitochondria. A,B HL-1 cells labelled for PK Mito (red) and F-actin (microfilament marker, green). Lipopolysaccharide (LPS) was continuously administered to HL-1 cells for 6 h, and then, images of cells were obtained using a Multi-SIM (High Sensitivity Structured Illumination Microscope; bar, 5 μm). For A and B, the enrichment degree of microfilaments on mitochondria and the movement rate of mitochondria after LPS treatment were calculated, respectively. To facilitate interpretation, the statistical results from Figure 1B are presented again in this panel. **C,D** HL-1 cells labelled for PK Mito (red) and F-actin (green). The white box shows the mitoFLARE structure of the mitochondria protruding from the microfilaments (C). Enrichment of microfilaments in HL-1 cells treated with LPS 20 μg and NEM 10 μM for 6 h (D). Images of cells were obtained using HIS-SIM (bar, 10 μm). **E** Protein levels of O-GlcNAc in HL-1 cells after LPS treatment. **F** The interaction between endogenous FHL2 and O-GlcNAcylated TRAK1 was detected via immunoprecipitation in HL-1 cells after LPS treatment. **G** Protein levels of FHL2 and TRAK1 in HL-1 cells after LPS treatment. **H** Schematic of redirection of the TRAK1–FHL2 complex onto the mitochondria. **I** HL-1 cells labelled for Tom20 (red) and FHL2 (green) antibody. Images of cells were obtained using HIS-SIM (bar, 5 μm). **J** HL-1 cells labelled for PK Mito (red) and F-actin (green). siRNA targeting FHL2 and TRAK1 prevented the enrichment of F-actin on mitochondria after LPS treatment. Images of cells were obtained using HIS-SIM (bar, 5 μm). Quantification of microfilament or FHL2 enrichment on mitochondria. $n = 5$ cells per condition from three independent transfections. The indicated P-values were derived from the two-tailed unpaired t test in which Welch's correction was used. a: $P < 0.05$ compared with the normal + si-CTRL group. b: $P < 0.05$ compared with the LPS + si-CTRL group. (Diagram was generated using Biorender).

actin filament network surrounding the mitochondria was formed in host cells (Fig. 2A and Video 12, 13). This structural alteration restricted mitochondrial motility, with mitochondria becoming trapped in an actin-constrained "nest-like" state, oscillating within a confined region, rather than undergoing long-range movement. Consequently, direct fusion-based mitochondrial communication was significantly impaired (Fig. 2B, Video 14). In response, mitochondria increased their reliance on long-distance nanotube-mediated communication (mitoFLARE) to compensate for the restricted direct fusion mode (Fig. 2C and Video 15) and may suggest the activation of an active endosymbiotic adaptation process. Further, the disruption of F-actin polymerisation significantly reduced mitoFLARE communication (Supplementary Fig. 1B, $P < 0.05$), whereas direct fusion-based communication was increased (Fig. 2D and Video 16, 17). In cytoskeletal research, NEM is renowned for its ability to effectively inhibit actin nucleation promoters such as fragmin and villin, thereby indirectly and effectively disrupting the polymerization process of F-actin[30]. These results indicate that actin network formation around the mitochondria restricts direct fusion, serving as a direct trigger for the transition to mitoFLARE -mediated communication.

Mechanistically, LPS stimulation increased cellular protein glycosylation modification, leading to glycosylation of the mitochondrial transport protein TRAK1 and its interaction with a mitochondria-anchoring protein FHL2 (Fig. 2E, F). This interaction was accompanied by an increased TRAK1 and FHL2 expression (Fig. 2G) and an enhanced mitochondrial anchoring of FHL2 (Fig. 2H, I). Notably, TRAK1 and FHL2 inhibition significantly reduced actin network formation around the mitochondria (Fig. 2J), with the knockdown efficiency of FHL2 and TRAK1 shown in Supplementary Fig. 1C, D. These findings may suggest that the binding of glycosylated TRAK1 to FHL2 is a key mechanism driving actin network formation around the mitochondria, which in turn plays a crucial role in switching mitochondrial communication from direct fusion to mitoFLARE during LPS treatment.

ER–Mito contact sites acting as "clamps" driving mitochondrial membrane protrusions and initiating mitoFLARE formation

To investigate the mechanism underlying mitoFLARE formation, as part of the mitochondrial adaptive response to actin network constraints in host cells, we conducted an in-depth analysis of mitoFLARE formation process. Mitochondrial "long filopodia" were not formed through simple elastic stretching of the outer and inner membranes. Instead, their elongation appeared originating from specific sites resembling "clamped" membrane contraction regions. Previous studies have indicated that Drp1-driven mitochondrial fission promotes mtDNA release, a process further mediated by BAX pore formation[31,32]. This is in line with our previous study[33] demonstrated that endoplasmic reticulum (ER)-Mito contact sites play a crucial role in marking mitochondrial membrane contraction points, a process closely associated with the mitochondrial fission protein Drp1.

To further investigate ER–Mito contact dynamics in LPS-treated myocardial cells, we constructed ER–Mito contact sensor plasmids (EML) and validated their functionality (Fig. 3A and Video 18). A significant increase in EML was seen in LPS treatment cardiomyocytes (Fig. 3B). At these contact sites, the mitochondrial outer membranes exhibited noticeable constrictions (Fig. 3C and Video 19, 20), which subsequently extended outwards to form the mitoFLARE structures (Fig. 3D). Live-cell imaging with dual labelling of the mitochondria and ER provided direct visual evidence of ER–Mito contacts facilitating mitoFLARE formation and elongation (Fig. 3E and Video 21). Additional imaging further confirmed that this process was closely linked to Drp1-mediated ER–Mito contact initiation (Fig. 3F and Video 22, 23), suggesting that Drp1-triggered ER–Mito contacts function as mitochondrial "clamps", providing the initiation sites for mitoFLARE formation.

To explore the molecular mechanisms undergoing this process, we examined the role of ER–Mito contacts in mitoFLARE formation. Under sustained LPS treatment, the number of EMLs gradually increased over time, while the average length of mitochondria progressively decreased (Supplementary Fig. 2A and Video 24). Meanwhile, increased ER–Mito contacts led to mitochondrial calcium overload (Fig. 3G), which subsequently upregulated the expression of a microtubule-associated motor protein KIF5A (Fig. 3H and Supplementary Fig. 2B), and enhanced its interaction with the mitochondrial outer membrane protein Miro1 (Fig. 3I). To dissect the role of calcium signaling in this pathway, we compared the general cytosolic calcium elevation induced by exogenous $CaCl_2$ addition with the specific calcium signal mediated by ER-mitochondria contacts upon LPS stimulation. As shown in Supplementary Fig. 2C, both treatments effectively activated KIF5A. Given that directly modulating calcium levels within the mitochondrial matrix would provide the most straightforward validation of the mechanism, we further examined whether inhibiting calcium transfer affects KIF5A expression and the frequency of mitoFlare. Knockdown of GRP75 led to a decrease in KIF5A expression and a reduction in mitoFlare occurrence, which aligns with our earlier findings. These results are presented in Supplementary Fig. 2D. Using optogenetic technique manipulation, the blue light-induced KIF5A-Miro1 binding (Fig. 3J and Supplementary Fig. 2E) significantly enhanced mitoFLARE elongation along microtubules and increased the number of mitoFLARE structures formed (Fig. 3K and Video 25), indicating that KIF5A–Miro1 pathway activation is a key mechanism driving mitoFLARE extension.

Early studies have demonstrated that the activation of Drp1 is a critical step in initiating endoplasmic reticulum–mitochondria contact formation, a process that depends on INF2-mediated polymerization of actin (F-actin) on mitochondria[33,34]. Furthermore, INF2 knockdown, which inhibited ER–Mito contact formation (Supplementary Fig. 2F, G), resulted in a remarkable reduction in mitochondrial calcium levels (Fig. 3G), decreased KIF5A expression and KIF5A-Miro1 binding (Fig. 3L, M), and significantly decreased mitoFLARE formation (Fig. 3N). Upon sh-INF2 treatment, live-cell imaging revealed that the disruption of the ER–mitochondria "clamp" largely prevented

https://doi.org/10.1038/s41467-026-73523-0

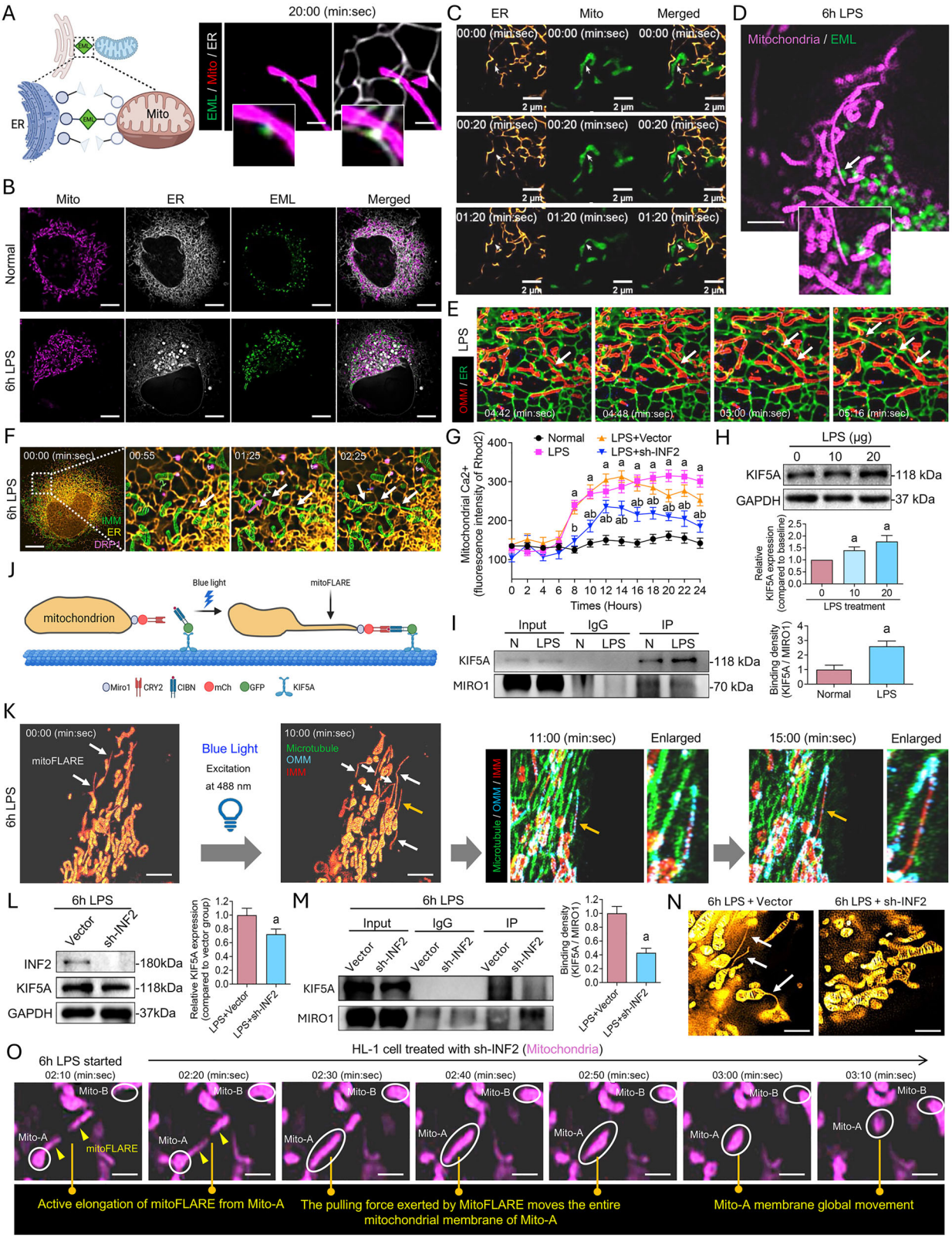

mitoFLARE formation (Supplementary Fig. 2H). As a result, the pulling force was aberrantly transmitted to the mitochondrial membrane, causing its global displacement. (Fig. 3O and Video 26, 27). These findings suggest that ER–Mito contacts likely function not only as initiation platforms for mitoFLARE formation but also serve to locally constrain and mechanically reinforce the site of membrane protrusion. This architecture, likely orchestrated by INF2-mediated actin nucleation, helps withstand the pulling force generated by the KIF5A–Miro1 complex and restricts force propagation to broader regions of the mitochondrial membrane. Consequently, ER–mitochondria contacts may facilitate the efficient conversion of motor protein activity into directed membrane tubulation rather than dissipative global movement, thereby promoting productive mito-FLARE assembly under LPS-induced inflammatory stress. Further

Fig. 3 | ER–Mito contacts as a "clamp" and initiate nanotube communication (mitoFLARE) formation, with the KIF5A–Miro1 pathway driving its extension. **A, B** A: Diagram of the ER and mitochondrial contact plasmid (EML). ER (white) and mitochondria (magenta) contact could be detected based on GFP fluorescence (green) (bar, 1μm). B: HL-1 cells after 6 h of lipopolysaccharide (LPS) treatment, images of cells were obtained using HIS-SIM (bar, 5 μm). **C** Time-lapse recording of continuous LPS administration to HL-1 cells using multi-SIM. HL-1 cells labelled to detect the ER (yellow) and mitochondria (green) (bar, 2 μm). **D** HIS-SIM was used to record the mitoFLARE (magenta) formation and across the EML structure (green) (bar, 2 μm). **E** HL-1 cells labelled for PK Mito (red) and ER (green). LPS was continuously administered to HL-1 cells for 6 h, and then, images of cells were obtained using an HIS-SIM. **F** HL-1 cells labelled for DRP1 (magenta), PK Mito (green), and ER (yellow). LPS was continuously administered to HL-1 cells for 6 h, and then, images of cells were obtained using a multi-SIM (bar, 5 μm). **G** Treatment with LPS potentiated mitochondrial Ca^{2+} uptake in HL-1 cells. Knocking down INF2 reduced the capture of Ca^{2+} by mitochondria. **H** Protein levels of KIF5A in HL-1 cells after LPS treatment. **I** The interaction between endogenous KIF5A and Miro1 was detected via immunoprecipitation in HL-1 after LPS treatment (means ± SD, $n = 3$ biologically independent samples). **J** Schematic illustration of mitoFLARE formation mediated by light-controlled mechanical stimulation. CRY2 fuses with Miro1 to target mitochondrial membranes, while CIBN fuses with a kinase motor protein encoded by KIF5A. Blue light regulates CRY2/CIBN dimerisation and induces kinase recruitment to the mitochondria, thereby exerting a pulling force on the mitochondria. **K** Fluorescence images of mitochondria in HL-1 cells after LPS treatment, with the HL-1 cells expressing CRY2-mCherry-Miro1 and Kif5A-GFP-CIBN (bar, 1 μm). **L** Protein levels of KIF5A and INF2 in sh-INF HL-1 cells after LPS treatment (means ± SD, $n = 3$ biologically independent samples). **M** The interaction between endogenous KIF5A and Miro1 was detected via immunoprecipitation in the sh-INF2 HL-1 cells line after LPS treatment (means ± SD, $n = 3$ biologically independent samples). **N** The formation of mitoFLARE in HL-1 cells decreased after knocking down INF2 (bar, 2 μm). **O** Time-lapse recording of sh-INF2 HL-1 cells continuously treated with LPS, using an HIS-SIM (bar, 1.5 μm). a: $P < 0.05$ compared with the normal group. b: $P < 0.05$ compared with the LPS + Vector group. (Diagram was generated using Biorender).

experimental results showed that LPS treatment significantly upregulated the expression levels of the key MAM proteins IP3R and VDAC, which may indicate one of the mechanisms by which LPS promotes ER–mitochondrial interactions (Supplementary Fig. 2I).

LPS treatment leads to mitochondrial inner–outer membrane anchoring loss, mitoFLARE dysfunction, and mtDNA redistribution

Under normal conditions, the inter-mitochondrial transfer of mtDNA relied on mitochondrial crista dynamics (Fig. 4A, Video 28). To explore the mechanism undergoing the gradual decline in mitochondrial inner membrane extension observed after 12 h of LPS treatment (Fig. 1F), we focused on changes in mitochondrial inner–outer membrane anchoring. Prolonged LPS stimulation significantly reduced the expression of the mitochondrial inner membrane-anchoring protein Mic19 (Fig. 4B, C), weakened Mic19–SAM50 interactions (Fig. 4D, E), and disrupted mitochondrial inner–outer membrane connectivity (Fig. 4D, E). These findings suggest that the loss of inner–outer membrane anchoring may contribute to the reduced capacity for inner membrane extension in mitoFLAREs.

Further investigation showed that Mic19 downregulation following 12 h LPS treatment triggered mitochondrial crista disorganization, resulting in the redistribution of mtDNA into localized aggregates and a reduction in mitoFLARE formation (Fig. 4F–H and Supplementary Fig. 3A). These results indicate that disruption of the MICOS–SAM complex is a key factor of the mitochondrial inner–outer membrane anchoring loss. This ultimately leads to mitoFLARE communication failure and aberrant mtDNA redistribution.

ER–Mito contacts promote mtDNA release and disrupting mitochondria–host cell symbiosis

Live-cell imaging showed that when the mitochondrial inner membrane extension was impaired and mitoFLARE communication was lost, a significant amount of Drp1 protein was then translocated along the ER to the ER–Mito contact sites, where it participated in mitoFLARE outer membrane rupture (Fig. 5A and Video 29, 30). This process involved the microtubule-mediated recruitment of Drp1 to mitochondria along the ER network (Fig. 5B and Video 31).

The recruited Drp1 was anchored to mitochondrial DNM2, severing the mitoFLARE outer membranes, thereby disrupting their integrity and exposing the mitochondrial matrix (Fig. 5C). Furthermore, high-resolution imaging using structured illumination microscopy (SIM) revealed that DRP1 accumulates at mitochondrial constriction sites and promotes the formation of mitoFLARE (Fig. 5D and Video 32). Super-resolution STORM imaging further confirmed that DRP1 forms ring-like structures at these constriction sites, which is associated with mitoFLARE generation (Supplementary Fig. 3B).

Additionally, Drp1, recruited to the mitoFLARE outer membrane, interacted with BAX channels on the mitochondrial membrane (Fig. 5E), facilitating the release of mtDNA and other mitochondrial matrix components into the host cell cytoplasm through BAX pores (Fig. 5F). Three-dimensional reconstruction further illustrated the process of mtDNA release from BAX pores on the mitochondrial outer membrane after 24 h of LPS treatment (Fig. 5G). This event may lead to complete breakdown of the mitochondrial–host cell endosymbiotic relationship. Moreover, the released mitochondrial matrix components can be recognized by host cells as DAMPs, triggering immune responses and exacerbating inflammatory damage. This finding may suggest that the Drp1-mediated mitochondrial fission machinery is essential for the dynamic formation of mitoFLARE.

Mitochondria–host cell symbiosis disruption triggering mtDNA-mediated activation of the STING pathway and may inducing immune responses and programmed cell death

Confocal microscopy demonstrated that after 24 h of LPS treatment, cytoplasmic mtDNA aggregates increasingly co-localised with cGAS and STING (Fig. 6A). Moreover, TBK1 and IRF3 phosphorylation levels were significantly elevated together with an increased expression of TNF-α and NLRP3 (Fig. 6B), indicating that the mtDNA released through BAX channels on the mitochondrial outer membrane activated the cGAS-STING pathway, promoting inflammatory cytokine release and inducing programmed cell death. To further demonstrate that mtDNA is readily recognized as a foreign substance, we performed additional experiments showing co-localization of mtDNA and cGAS upon mitochondrial membrane rupture. These findings indicate that LPS-induced disruption of the mitochondrial membrane leads to exposure of internal mtDNA and activation of cytosolic innate immune sensing pathways, such as cGAS. The corresponding results have been included in Supplementary Fig. 3C.

Additionally, we observed significant deficiencies in the lysosomal degradation of mitochondrial debris in the LPS-treated cells compared to that of the controls (Fig. 6C and Video 33, 34), suggesting impaired mitophagy flux during LPS treatment. Under these conditions, lysosomes did not efficiently degrade mitochondria-released mtDNA owing to mitophagy dysfunction, which may lead to persistent immune activation (Fig. 6D and Video 35, 36). This ultimately disrupted, for example, cardiac tissue homeostasis and exacerbated inflammatory responses.

Notably, Drp1 knockdown at the cellular level significantly mitigated LPS-induced activation of the cGAS-STING pathway (Fig. 6E). Further experiments using Drp1-knockout mice revealed that cardiac inflammation in sepsis was markedly reduced compared to that in wild-type mice (Fig. 6F, G). Efficiency of cardiac-specific DRP1

https://doi.org/10.1038/s41467-026-73523-0

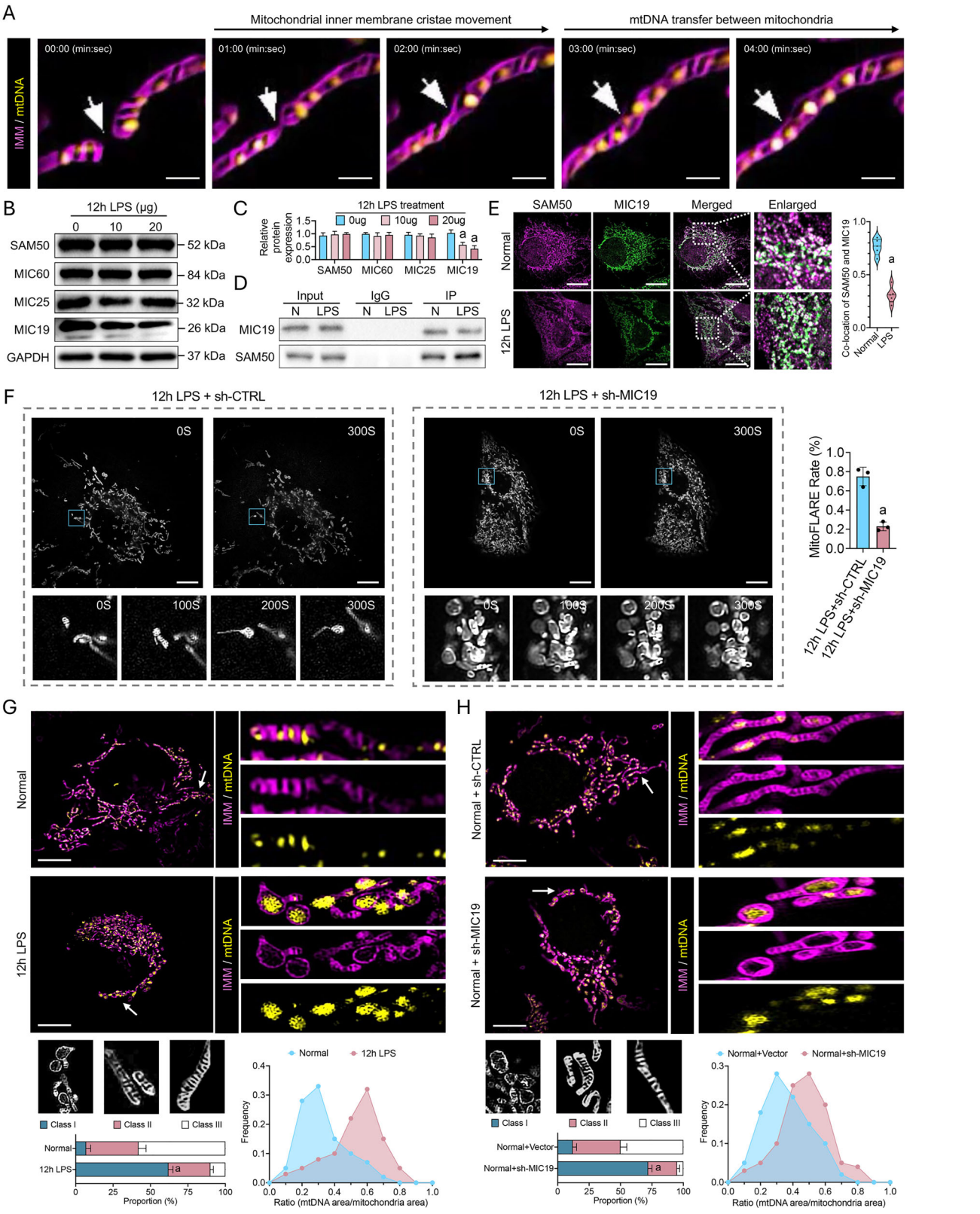

knockout is shown in Supplementary Fig. 3D. Moreover, the preservation of cardiac contractile function and strain capacity was significantly improved in the CLP Drp1-knockout mice compared to that in the CLP wild-type mice (Fig. 6H). This was accompanied by enhanced EF and FS (Supplementary Fig. 3E, F), in addition to a significant decrease in the cardiomyocyte apoptotic rate (Fig. 6I). Consistently, knockdown of DRP1 significantly reduced the occurrence of mitoFLARE, supporting its functional role in this process (Supplementary Fig. 3G).

Discussion

The tubular mitochondrial extensions initially described as "nanotunnels" provided an important conceptual foundation for understanding long-distance mitochondrial communication (Bernardini

Fig. 4 | LPS treatment disrupts the MICOS–SAM complex, leading to mitochondrial membrane detachment, nanotube communication (mitoFLARE) failure, and mitochondrial DNA (mtDNA) redistribution. A HL-1 cells labelled for PK MITO (magenta) and mtDNA (yellow). Time-lapse recording the mtDNA transfer in HL-1 cells using a High Sensitivity Structured Illumination Microscope (Multi-SIM, Scale bar: 1 μm). **B** Protein levels of MIC19, MIC25, MIC60, and SAM50 in HL-1 cells after lipopolysaccharide (LPS) treatment. **C** is statistical analysis corresponding to (B) (means ± SD, $n = 3$ biologically independent samples). **D** The interaction between endogenous MIC19 and SAM50 was detected via immunoprecipitation in HL-1 cells after LPS treatment (through SAM50 antibody IP). **E** After LPS treatment, HL-1 cells were labelled for SAM50 (magenta) and MIC19 (green). Scale bar: 5 μm. **F** Representative fluorescence images of mitochondria in HL-1 cells transfected with sh-MIC19 or sh-control, followed by treatment with LPS (20 μg/mL) for 12 h. Mitochondria were labeled with PKmito. Scale bar: 5 μm. **G**, **H** Frequency distribution of the ratio of mtDNA area to mitochondrial area. HL-1 cells labelled for PK Mito (magenta) and mtDNA (yellow). The distribution of mtDNA in mitochondria after LPS treatment and the distribution of mtDNA after MIC19 knockdown were observed in HL-1 cells. Scale bar: 5 μm. a: $P < 0.05$ compared with the control group.

et al., BBRC 2008[19]; Huang et al., PNAS 2013[20]). Building on these observations, our study demonstrates that these structures are physiologically present but become abundant and undergo dynamically regulated transitions under inflammatory stress. Rather than redefining this phenomenon, our findings extend the current concept of mitochondrial nanotunneling by elucidating their regulatory mechanisms, structural dynamics, and functional consequences. Thereby, systematically addressing key unresolved questions in the field[21]: First, we delineated the dual-membrane dynamics of mitoFLARE and identified inner membrane integrity as critical for nanotunnel function, with compromised inner membrane extension leading to outer membrane "ghost" formation and subsequent leakage. Second, we uncovered the mechanism involving TRAK1 glycosylation and the FHL2 axis that drives perimitochondrial actin network remodeling, explaining how mitochondria establish immobilized nanotunnels for long-distance communication. Third, we elucidated the dual role of ER–Mito contact sites as "clamps" driving nanotunnel initiation and extension, demonstrating that the ER serves not only as a fission platform but also as a structural basis for tunnel formation. Fourth, we identified disruption of the MICOS–SAM complex as the structural basis for impaired inner membrane extension under sustained stress, resulting in cristae disorganization and aberrant mtDNA distribution. Fifth, we revealed that DRP1-BAX axis-mediated outer membrane rupture of nanotunnels and subsequent mtDNA release directly link nanotunnel failure to cGAS-STING pathway activation and septic immune storm. Collectively, these findings expand our understanding of mitochondrial nanotunneling—from structural dynamics and molecular regulation to functional outcomes—and elucidate the mechanisms underlying mitoFLARE formation under inflammatory conditions[35].

However, the term "nanotunneling" is etymologically rooted in intercellular communication structures with cytoskeletal cores[36,37], which does not accurately reflect the intrinsic, membrane-only composition of these organelle-derived structures that we observed. We, therefore, propose the more precise and descriptive term "mitoFLARE" (Mitochondrial Flagella-like Extensions) precisely describe this stress-induced and abundantly formed mitochondrial nanotunneling. It exhibits flagella-like membranous extensions without cytoskeletal support and, more importantly, emerges in an inducible, flare-like manner under pathological stress. In this study, the dynamic evolution of the mitochondria–host cell endosymbiotic relationship, from compensatory adaptation to decompensated collapse during sepsis, was systematically determined in this study through multi-experimental settings, including molecular probe labelling and optogenetic manipulation. Our data showed that during the active adaptation phase, mitochondria shift their mode of communication from direct fusion to nanotube communication (mitoFLARE) in response to mild LPS treatment. In the dysregulation phase, progressive inflammation induces MICOS–SAM complex damage, the loss of inner–outer membrane anchoring, mitochondrial outer membrane rupture, and mtDNA release, activating the cGAS-STING pathway, triggering immune dysregulation and inflammatory storms (Fig. 7). Ultimately, this cascade leads to programmed cell death and contributes to organ dysfunction. By building upon established knowledge of mitochondrial quality control imbalance and cGAS-STING pathway activation[38] as well as previous reports on Drp1 targeting in septic cardiomyopathy[39], our study further elucidates the intrinsic link between mitochondrial homeostasis and immune dysregulation under septic conditions. These findings provide additional theoretical insights into the progression of sepsis, potentially revealing therapeutic targets for intervention.

Under inflammatory conditions such as sepsis, mitochondrial dynamics undergo a significant shift in motility, which serves not as a passive consequence but as a critical adaptive precursor, activating what is termed the "active endosymbiotic adaptation process"—a concept rooted in the bacterial origin of mitochondria whereby, under stress, mitochondria reactivate α-proteobacterial survival strategies by forming flagella-like membrane protrusions called mitoFLARE[40,41]. Similar to bacterial flagella enabling environmental exploration, these extensions allow mitochondria to establish connections with neighboring organelles, facilitating content exchange, damage sequestration, and signal coordination to maintain function and survival in harsh microenvironments, reflecting a programmed adaptive mechanism deeply embedded in their evolutionary heritage.

Sepsis significantly altered mitochondrial dynamics and increased mitochondrial fission, while reducing fusion and biogenesis[42]. However, the underlying mechanisms remain unclear. Our study demonstrated that during early inflammation, mitochondrial motility is restricted, shifting from long-range rapid movement to short-range oscillations. A previous study demonstrated that a bundled actin network limited direct mitochondrial fusion and communication, whilst the binding of glycosylated TRAK1 to FHL2 was considered to be a key driver of that actin network formation[43]. In line with this, our data revealed that LPS-induced damage led to a significant increase of TRAK1 and FHL2 expression, as well as enhanced glycosylated TRAK1–FHL2 interactions. FHL2 is the most abundantly expressed in the heart, vasculature, ovaries, and skeletal muscle but a relatively low expression in other organs and plays a critical role in regulating signal transduction in various diseases, including cardiomyopathy, aging, and diabetes[44,45]. Interestingly, recent studies showed that FHL2 anchored actin filaments to the mitochondria, restricting their movement[43]. TRAK1, which connects to microtubules via kinesin proteins, is tightly associated with FHL2 and forms a complex network that further constrains mitochondrial mobility[46]. These findings suggest that glycosylated TRAK1–FHL2 binding may serve as a key trigger for actin network formation, providing a structural foundation for mitochondria to be active of their modes of communication. Subsequently, mitochondria establishing long-distance communication through nanotube-like structures, known as mitoFLAREs, facilitates the exchange of inner membrane matrix components that are closely linked to ER–mitochondrial contacts. Previous studies demonstrated that mitoFLAREs emerged when elongated mitochondria actively reached dynamic ER networks[47]. However, our current work reveals a different mechanism that ER–mito contacts may act as a "clamp", driving the formation of mitochondrial membrane protrusions and initiating mitoFLARE formation (Fig. 3D–F). This process was further validated through a fluorescent protein-splitting system, which specifically marks ER–mito contacts. Additionally, mitoFLARE elongation

https://doi.org/10.1038/s41467-026-73523-0

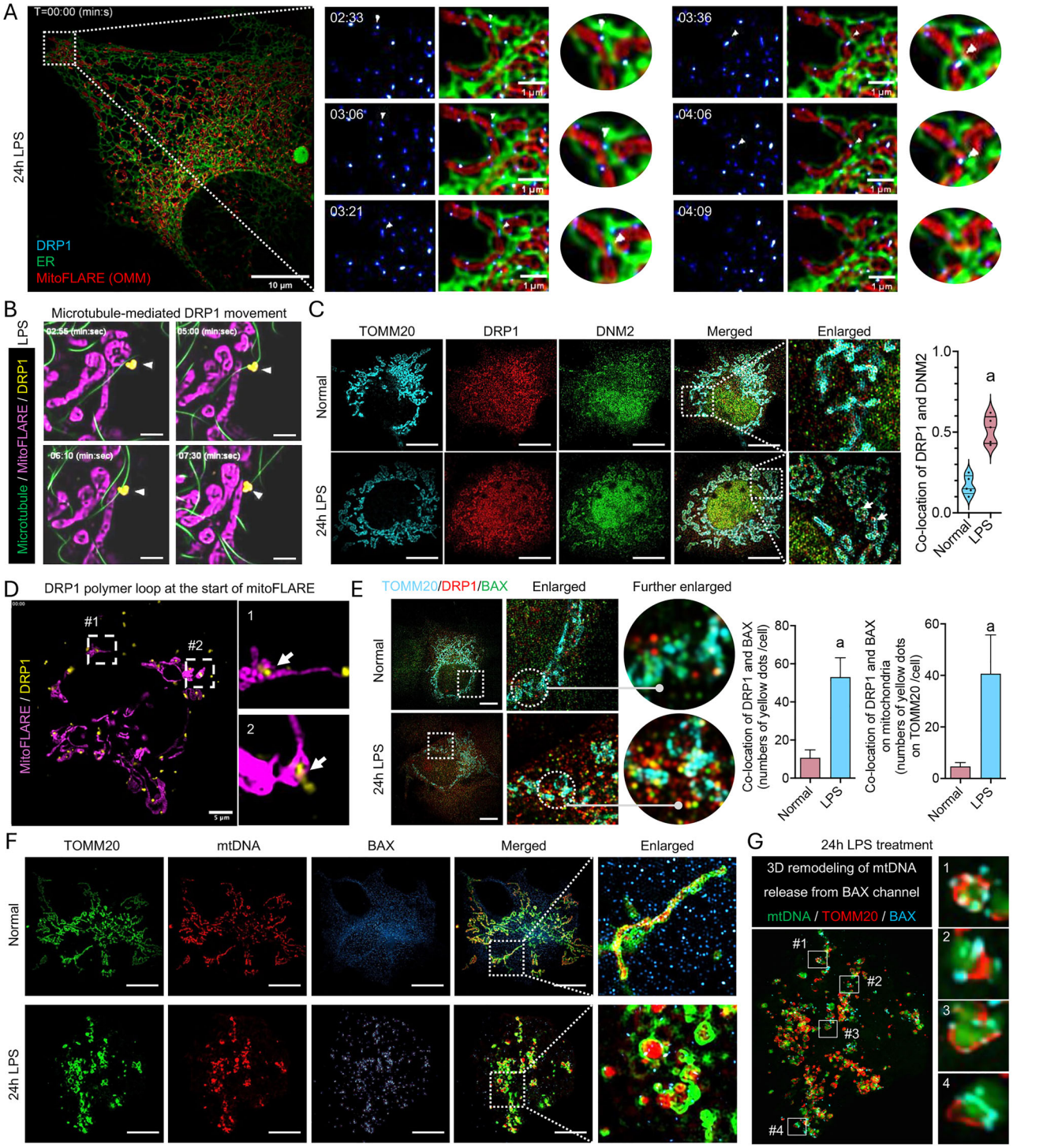

Fig. 5 | ER–Mito contacts recruit Drp1 to activate the BAX channel, triggering mitochondrial DNA (mtDNA) release and disrupting mitochondria–host cell symbiosis. A HL-1 cells labelled for DRP1 (cyan), ER (green), and PK Mito (red). Lipopolysaccharide (LPS) was continuously administered to HL-1 cells for 24 h, and then, images of cells were obtained using a HIS-SIM (Scale bar: 10 μm). **B** HL-1 cells labelled for DRP1 (yellow), tubulin (green), and PK Mito (magenta). LPS was continuously administered to HL-1 cells for 24 h, and then, images of cells were obtained using a High Sensitivity Structured Illumination Microscope (Multi-SIM) (Scale bar: 1 μm). **C** After LPS treatment, HL-1 cells were labelled for TOM20 (cyan), DRP1 (red), and DNM2 (green) (bar, 10 μm). **D** HL-1 cells labelled for DRP1(green), PK Mito (magenta). LPS was continuously administered to HL-1 cells for 6 h, then images of cells were obtained using a Multi-SIM (bar, 5 μm). **E** After LPS treatment, HL-1 cells were labelled for TOM20 (cyan), DRP1 (red), and BAX (green) (means ± SD, $n = 3$ biologically independent samples) (bar, 5 μm). **F** After LPS treatment, HL-1 cells were labelled for TOM20 (green), mtDNA (red), and BAX (cyan) (bar, 10 μm). **G** 3D reconstruction of LPS group of (F). HL-1 cells labelled for TOM20 (red), mtDNA (green), and BAX (cyan). a: $P < 0.05$ compared with the normal group.

https://doi.org/10.1038/s41467-026-73523-0

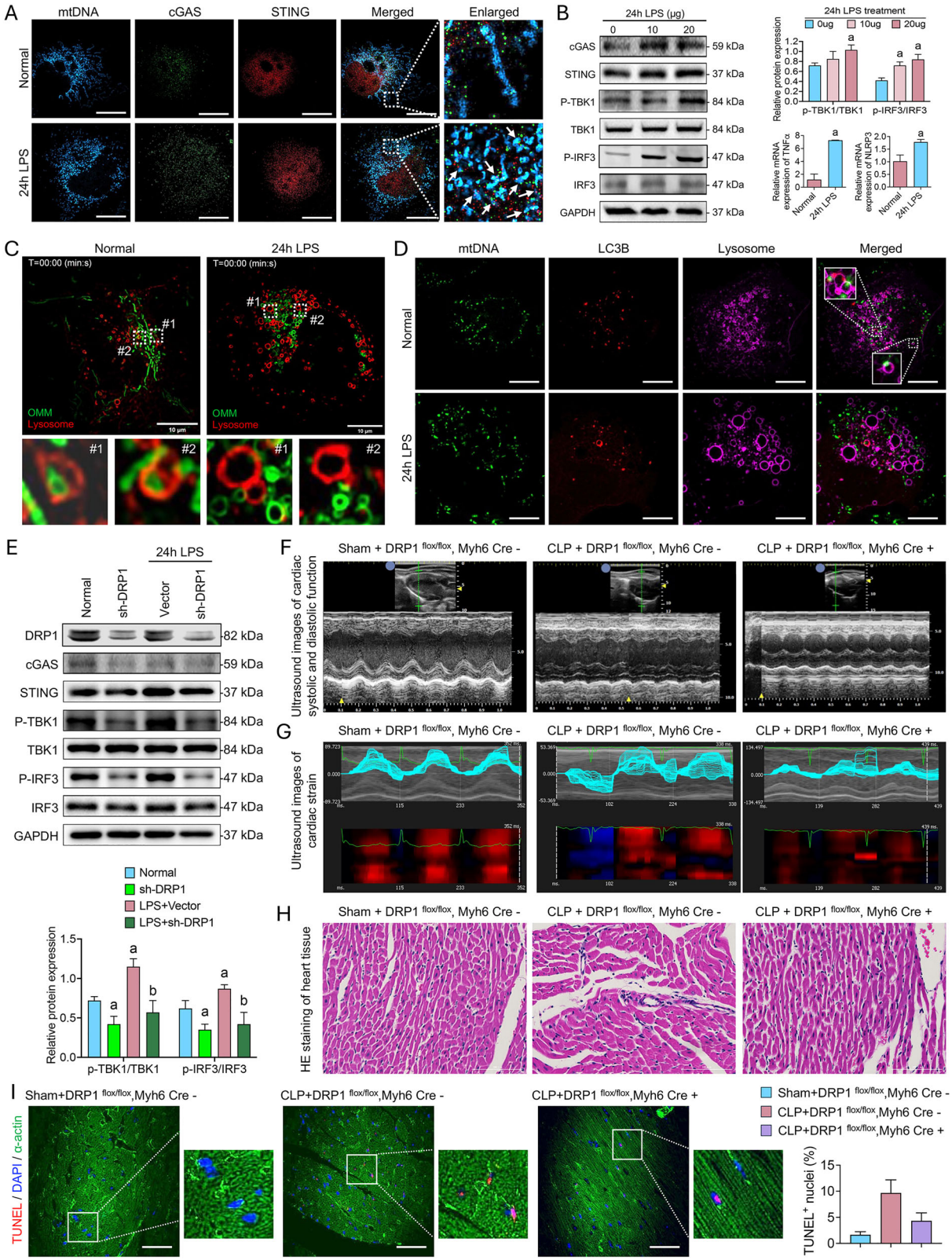

relies on activation of the KIF5A–Miro1 pathway, which directs mitochondrial membrane protrusions along microtubules, ultimately forming the nanotube structure. Using optogenetics, we further confirmed that mitoFLARE formation was dependent on the interaction between KIF5A and Miro1.

As inflammation progress, mitochondrial membrane integrity is significantly deteriorated, leading to the dysregulation of mitochondria–host cell homeostasis. A hallmark of this disruption is the loss of the dynamic coordination between the inner and outer mitochondrial membranes. Previous studies showed that the MICOS–SAM complex plays a crucial role in tethering the inner and outer mitochondrial membranes and that MICOS directly influenced the structural organisation of the inner membrane[48]. Our study revealed that Mic19 expression was impaired in the LPS-treated cells,

Fig. 6 | Mitochondrial DNA (mtDNA) release as a damage-associated molecular pattern (DAMP) signal activates the cGAS-STING pathway, inducing an immune response and programmed cell death. A After lipopolysaccharide (LPS) treatment, HL-1 cells were labelled for mtDNA (cyan), cGAS (green), and STING (red) (bar, 10 μm). **B** Levels of cGAS-STING pathway proteins in HL-1 cells after LPS treatment (means ± SD, $n = 3$ biologically independent samples). **C** HL-1 cells labelled with TOMM20(green) or lysosomes (red) in HL-1 cells after LPS treatment. **D** HL-1 cells labelled for mtDNA (green), LC3B (red), or lysosomes (magenta) in HL-1 cells after LPS treatment. **E** Levels of cGAS-STING pathway proteins in sh-DRP1 HL-1 cells after LPS treatment (means ± SD, $n = 3$ biologically independent samples). **F–H** Echocardiography (F and G) and HE staining (H) using DRP1-knockout mice after CLP modelling (means ± SD, $n = 3$ biologically independent samples). **I** Images of heart sections stained with TUNEL (red), anti-α-actin (green), and DAPI (blue) and the percentages of TUNEL-positive nuclei using DRP1-knockout mice after CLP modelling (means ± SD, $n = 3$ biologically independent samples). a: $P < 0.05$, compared with the normal group. b: $P < 0.05$, compared to the LPS + vector group.

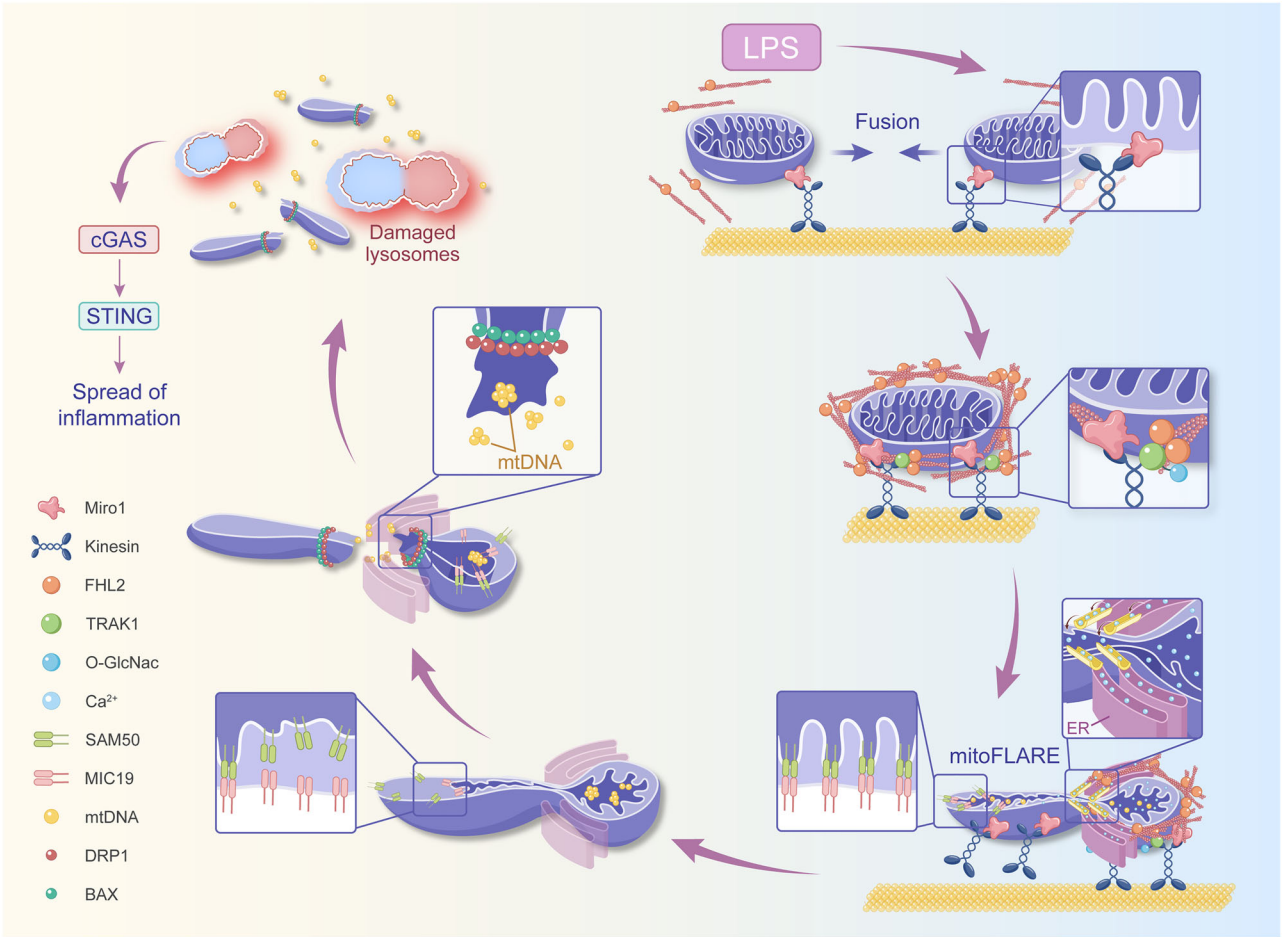

Fig. 7 | Proposed model of LPS-driven mitoFLARE dysfunction leading to mtDNA release and cGAS-STING activation. This study revealed the dynamic transition of mitochondria-host cell symbiosis from adaptive compensation to pathological dysregulation during sepsis progression. In the early phase (0–6 h), LPS treatment alters mitochondrial motility, inducing a shift from long-distance rapid movement to short-range oscillations and restricting direct fusion-based communication. To compensate for this, mitochondria establish mitoFLARE-mediated nanotube communication driven by glycosylated TRAK1/FHL2-induced actin remodelling and ER–Mito contact-driven membrane protrusion formation, which is further extended via the KIF5A–Miro1 pathway. However, as inflammation intensifies (6–24 h), mitochondrial quality control fails, leading to disruption of the MICOS–SAM complex, the loss of inner-outer membrane anchoring, and mitoFLARE dysfunction. ER–Mito contacts recruit DRP1 to mitochondrial constriction sites, facilitating outer membrane fission through DNM2, whereas the DRP1-mediated activation of BAX channels results in the release of mitochondrial DNA (mtDNA) into the cytosol. The released mtDNA acts as a damage-associated molecular pattern (DAMP) signal, triggering the cGAS-STING pathway, amplifying the immune response, inducing programmed cell death, and exacerbating inflammation and tissue damage. mitoFLARE: mitochondrial flagella-like extensions; mtDNA: mitochondrial DNA; ER: endoplasmic reticulum. (Diagram was generated using Adobe Illustrator 2023).

leading to a significant reduction in its interaction with SAM50. This weakened the MICOS–SAM complex and disrupted mitochondrial membrane anchoring, compromised inner membrane extension, and ultimately resulted in nanotube-mediated communication failure. The reduction of Mic19 expression emerges as a key molecular event in this process, and this is accompanied by the loosening of mitochondrial crista structures. We further validated this by directly knock-down Mic19 expression, confirming its role in maintaining crista integrity. It was demonstrated that mitochondrial damage led to the loss of the characteristic crista barrier structure, causing mtDNA to shift from an organised distribution to localised accumulation[49]. In addition, our study revealed that mtDNA accumulation is closely associated with disruption of the MICOS–SAM complex. Further, the loss of membrane anchoring destabilises the inner mitochondrial crista structure and facilitates mtDNA aggregation. Building upon these findings, it is important to clarify that while both the pathological redistribution of mtDNA and the formation of mitoFLARE structures originate from the common upstream event of Mic19 downregulation and subsequent

MICOS–SAM complex disruption, they represent independent, parallel consequences of this compromised membrane integrity. Structurally, the impaired inner membrane extension directly hinders the proper formation and function of mitoFLARE, and although these membrane extensions can secondarily envelop the pre-existing aggregated mtDNA, the essential communication function of mitoFLARE is itself compromised, indicating no direct causative relationship between the two phenomena.

We firmly establish that DRP1-mediated mitoFLARE formation drives mtDNA release and subsequent STING activation, thus validating the central role of this entire axis in the disease pathogenesis. ER–mitochondria contacts recruit DRP1 to mitochondrial membrane constriction sites, leading to detached outer membrane fragments. During this process, DRP1 interacts with BAX channels, resulting in the release of mitochondrial matrix components, including mtDNA, into the cytoplasm via BAX pores, which is consistent with previous findings[31,50]. Once in the cytoplasm, mtDNA acts as a DAMP signal, activating the cGAS-STING pathway, which catalyses cGAMP production and triggers the TBK1-IRF3 signalling cascade. This, in turn, promotes the expression of type I interferons and pro-inflammatory cytokines[51]. Ultimately, these inflammatory mediators induce programmed cell death via apoptosis or pyroptosis, further exacerbating inflammation and contributing to organ dysfunction.

The pathophysiological hallmark of sepsis is a dysregulated systemic response to infection with immune dysfunction as the core pathological mechanism. This immune dysregulation triggered by infection results in self-inflicted damage to host cells and organs[52]. When pattern recognition receptors, including Toll-like receptors, within the innate immune system are activated, they initiate inflammatory cascades by triggering the release of NF-κB and type I interferons, ultimately leading to immune activation and subsequent damage host tissues/organs[52]. An imbalance in mitochondrial quality is a key driver of immune dysregulation, with mtDNA release and activation of the cGAS-STING pathway playing a central role in this process[53]. The sepsis-induced release of mtDNA and subsequent development of SIRS[54] are major contributors to myocardial injury and multi-organ failure in affected patients. The disruption of mitochondria–host cell symbiosis may be the pathology of sepsis in the advanced disease stage. Mitochondrial mobility is restricted, which limits direct fusion events. To overcome the actin cytoskeletal "nest" barrier[55], mitochondria actively extend protrusions to establish material exchange with other mitochondria or organelles, facilitating mitoFLARE-mediated communication. However, as inflammation progresses, mitochondria–host cell homeostasis becomes increasingly disrupted. The loss of inner and outer mitochondrial membrane anchoring reduces effective mitoFLARE communication. Consequently, the isolated extensions of the outer mitochondrial membrane are recognised and severed by DRP1, leading to the release of mtDNA from the inner membrane into the host cytoplasm. This event triggers immune decompensation and a severe inflammatory storm. Thus, the symbiotic relationship between the mitochondria and host cells is fundamental for maintaining cellular homeostasis. An imbalance in mitochondrial quality initiates an immune storm, accelerates the progression of sepsis, and exacerbates organ dysfunction.

This study systematically elucidated the molecular mechanisms by which mitochondria maintain endosymbiotic homeostasis under LPS treatment through dynamic transitions in the communication mode, as well as the pathways leading to its dysregulation. However, several limitations require further investigation. First, our experimental model primarily relies on LPS-induced in vitro cellular inflammation model although clinically revelant sepsis model was also included. The complex multiorgan and multicellular interactions that occur during sepsis progression require further study; consequently, the precise role and regulatory network of mitoFLARE within the intact organism, particularly its response to systemic inflammatory signals, remain to be fully elucidated. These limitations highlight that our current findings, while foundational, necessitate validation in more complex in vivo systems to comprehensively define the pathophysiological significance of mitoFLARE in sepsis. In particular, tissue-specific mitochondrial responses require validation based on organoid and animal models. Second, although we uncovered the molecular basis of TRAK1 glycosylation-mediated interactions with FHL2 in driving actin network remodelling, the precise roles of specific glycosyltransferases and their spatiotemporal regulation remain unclear. A systematic analysis integrating proteomics and live-cell imaging is required to elucidate these further. Third, the mechanotransduction mechanisms underlying ER–Mito contact-mediated mitoFLARE formation remain unclear. Our current study primarily focused on mitochondrial calcium signalling and the KIF5A axis; However, the interplay between mitochondrial membrane tension and ER crista remodelling requires further clarification using biophysical approaches, such as mechanosensitive microscopy. Lastly, our study primarily focused on the intrinsic adaptive mechanisms of mitochondria, but the impact of host cellular metabolic reprogramming (e.g. enhanced glycolysis) on mitochondrial communication remains unknown and warrants further study.

In summary, our study revealed that disruption of the mitochondria–host cell endosymbiotic relationship drives sepsis progression through mitochondrial dysfunction and mtDNA-mediated inflammation. Therefore, preserving mitochondria–host cell symbiosis may serve as a potential therapeutic strategy for treating septic-related organ injury, including cardiomyopathy.

Methods

Animal experiments and cell culture

Animal care and experimental protocols were reviewed and approved by the Institutional Animal Care and Use Committee of the Second Affiliated Hospital of Chongqing Medical University [Approval No. 2022 (222)], Chengqing, China. C57/BL6 male mice were purchased from Beijing Vital River Laboratory Animal Technology Co., Ltd, Beijing, China, and Drp1-knockout C57BL/6J mice (Drp1 flox/flox) were generated using CRISPR/Cas9 technology (ShanghaiModel Organisms Center, Inc. Shanghai, China). Myh6-cre mice were purchased from The Jackson Laboratory (stock number: 011038) and crossed with Drp1-knockout mice to generate cardiomyocyte-specific Drp1-knockout mice (DRP1 flox/flox, Myh6 cre+). Only male mice were utilized in the experiments.

Mice were housed under pathogen-free conditions and maintained at 22 °C with 50% relative humidity and a 12 h alternating light/dark cycle. The cecal ligation and puncture (CLP) model was established by ligating the distal portion of the cecum (75%–80% of its length), followed by a single through-and-through puncture with a 20-gauge needle to induce polymicrobial sepsis under surgical anesthesia as reported previously[56]. Mice were monitored for 24 h post-CLP, after which heart tissue samples or outcome parameters were collected for analysis.

HEK293T and HL-1 cells were obtained from HyCytes and cultured in Dulbecco's modified Eagle medium (DMEM; Gibco, C11995500CP) supplemented with 10% foetal bovine serum (FBS; Gibco 10091155) and 50 U/mL penicillin/streptomycin (Gibco; 15140122) at 37 °C in an incubator with 5% CO_2. HL-1 cells were treated with various concentrations (0, 10, 20 μg/mL) of LPS for 6 h to 24 h[57]. A dose of 20 μg/mL was selected to induce mitoFLARE formation based on previous studies demonstrating that this concentration effectively induces cellular stress and functional suppression[58]. Stable Mic19-, DRP1-, and INF2-knockdown cell line transfectants were established using a lentiviral system, as described previously[59]. Briefly, the plasmid was co-transfected into HEK293T cells with packaging plasmids (pMD2.G and psPAX2). After 48 h, the culture medium was mixed with HitransG P viral infection reagent (Genechem, REVG005) to infect HL-1 cells. To

generate stable cell lines, HL-1 cells were selected using puromycin (10 μg/mL). The sequences were as follows: shNC (negative control), 5′-TTCTCCGAACGTGTCACGT-3′, 3′-AAGAGGCTTGCACAGTGCA-5′; shMIC19, 5′- TCTGCTCTGGCTAGCCAATAC-3′, 3′-AGACGA-GACCGATCGGTTATG-5′. Lentiviral vectors carrying the mouse *DRP1* gene-knockdown construct were obtained from GeneCopoeia. Lentiviral vectors carrying the mouse *INF2* shRNA was obtained from VectorBuilder.

Western blotting and RT-qPCR

The treated or controlled cells were lysed in RIPA buffer. Proteins in the supernatant were then extracted following centrifugation at 13,000 × *g* for 15 min at 4 °C. The extracted proteins were separated using sodium dodecyl sulphate-polyacrylamide gel electrophoresis and subsequently transferred onto nitrocellulose membranes. Membranes were blocked with 1 × TBST containing milk powder for 1 h and incubated with primary antibodies at 4 °C overnight. GAPDH was used as an internal control. After three washes with 1 × TBST for 7 min each, the membranes were analysed using the ECL detection system.

Total RNA was isolated from cells using the Eastep Super Extraction Kit (LS1040, Promega) according to the manufacturer's instructions. The isolated RNA was then reverse-transcribed into cDNA using the PrimeScript RT Master Mix (Perfect Real-Time). Quantitative analyses were performed using the SYBR Green 2 × PCR Master Mix (06924204001; Roche, Basel, Switzerland) on a Bio-Rad CFX system. The primers used for RT-qPCR are listed in Supplementary Table 1.

Structured illumination microscopy (SIM) and Nanolive optical diffraction tomography (ODT) live-cell imaging

HL-1 cells were seeded onto confocal dishes (D35-20-1.5-N; CellVis) and incubated overnight. After transfecting the cells with the corresponding fluorescent plasmids for 24 h, medium was replaced with fresh medium containing 20 μg/mL LPS, and the treatment proceeded for the specified duration. Live-cell imaging was performed using a SIM microscope. Sustained blue light stimulation was delivered using pulsed illumination (200 ms pulses at 10-s intervals) to target cells. The CRY2-mCherry-Miro1 and Kif5A-GFP-CIBN plasmids were procured from Addgene (via Lab Cell) for optogenetic manipulation.

For Nanolive ODT, HL-1 cells were seeded onto glass-bottomed dishes (35 mm, Ibidi, cat. no. 81218-200) and incubated overnight. The following day, the cell culture medium was replaced with fresh medium containing 20 μg LPS to mimic the sepsis-induced myocardial injury process. Throughout the imaging process, cells were maintained at 37 °C in a 5% CO_2 atmosphere in a temperature-controlled incubation chamber. After 6 h of LPS treatment, one frame was captured every 10 s for a continuous 5 min period. Live-cell imaging was conducted using a 3D Cell Explorer microscope (Nanolive), via ODT, equipped with Evev1.8.2 software.

Transmission electron microscopy (TEM) imaging

Fresh heart tissues from CLP mice after 1 day of sepsis being established or controls were fixed in an arsenate buffer containing 2.5% glutaraldehyde for 24 h at 4 °C (pH 7.4). After three 10 min washes with 0.13 M PBS, the tissues were post-fixed with 1% osmium tetroxide for 2 h at 25 °C. The samples were then dehydrated in a graded ethanol series (65%, 70%, 75%, 80%, and 95% for 10 min each). Subsequently, the tissues were incubated with tert-butoxide for 10 min and then dried under CO_2. Finally, images were captured using TEM.

Mitochondrial calcium ion detection assay

Briefly, cells were seeded onto a 96-well plate and incubated overnight. The following day, culture medium was replaced with fresh medium containing 20 μg LPS to mimic the sepsis-induced myocardial injury process. Cells were maintained at 37 °C in a 5% CO_2 atmosphere in a temperature-controlled incubation chamber. After LPS treatment at different time points, cells were processed according to the manufacturer's instructions. After adding 100 μL of Rhod-2 staining solution, the cells were incubated at 37 °C for min, followed by supernatant removal, PBS washing (twice), and fluorescence intensity measurements using a BioTek CYTATION5 multi-mode microplate reader. Data were analysed using Bio-Rad CFX Manager software and GraphPad Prism 9.

Co-immunoprecipitation (Co-IP) assays

Co-IP assays were performed according to established protocols. Briefly, cells were lysed in ice-cold Tissue IP Lysis Buffer (supplemented with a protease inhibitor cocktail) and homogenised through vortexing. After centrifugation at 13,000 × *g* for 15 min at 4 °C to pellet the cellular debris, the supernatant was divided into three aliquots, as follows: one was preserved as the input control, two experimental groups were incubated overnight at 4 °C with either (a) an anti-FHL2 antibody (1:200) or anti-KIF5A antibody (1:200) for co-precipitation or (b) a species-matched normal IgG isotype control antibody (1:200) (proteintech, Wuhan, China). Protein complexes were captured by adding 30 μL Protein A/G Agarose Beads to each sample with a 4 h rotation at 4 °C. The beads were pelleted via centrifugation (2000 × *g*, 1 min), washed seven times with ice-cold PBS (pH 7.4), and resuspended in 2× Laemmli buffer for subsequent immunoblotting.

Immunofluorescence

HL-1 cells were cultured in glass-bottom dishes using DMEM. After LPS (20 μg) induction, cells were fixed at room temperature with 4% paraformaldehyde for 10 min. The cells were permeabilised with 1% Triton-X 100 in PBS at room temperature for 10 min and blocked with 5% BSA at room temperature for 30 min. Subsequently, cells were incubated with primary antibodies diluted in 5% BSA at 4 °C overnight. After overnight incubation with the primary antibody, the cells were washed three times with PBS and incubated with secondary antibodies in 5% BSA at room temperature for 1 h. The following secondary antibody was used: Cy3-conjugated donkey anti-rabbit IgG (H + L) (1:800; #111-165-003, Jackson). Finally, the cells were washed three times with PBS, and the plates were imaged using an HIS-SIM confocal microscope.

Live-cell fluorescence imaging

Briefly, HL-1 cells were seeded onto confocal dishes (D35-20-1.5-N; CellVis) and incubated overnight. The cells were then transfected for 24 h using Lipofectamine™ 3000 (Lipo3000) with 1.5 μg of the respective fluorescent plasmids to label various organelles: TOM20-GFP for the mitochondrial outer membrane, Tubulin-GFP for microtubules, F-actin-GFP for microfilaments, Calnexin-mCherry for the endoplasmic reticulum (ER), LC3B-mCherry for autophagosomes, and LAMP1-GFP for lysosomes. The EML plasmid was used to label ER–mitochondria contacts. Following transfection, the medium was replaced with fresh medium (LPS was added at this point if required, followed by the corresponding treatment duration). At 24 h post-transfection, cells were stained with PK Mito (1:2000 dilution) for 15 min to label the mitochondrial inner membrane, and with SYBR™ Gold dye (Thermo Fisher; 1:10000 dilution) for 15 min to visualize mitochondrial DNA.

Measurement of MitoFLARE Rate

In this study, the identification and quantification of mitoFLARE structures were performed according to strict and reproducible criteria, building upon a previously established methodology[47]. mitoFLARE was defined as an elongated tubular extension protruding from the main mitochondrial body, with a length significantly exceeding its diameter. The connection site between the mitoFLARE and the mitochondrial body was identified as a narrow constriction zone (diameter <300 nm) adjacent to the spherical portion of the mitochondrion.

Image Processing and Mitochondrial Area Quantification

Mitochondrial areas were assessed using trainable WEKA segmentation implemented in Fiji, followed by image binarization. Subsequently, threshold-based segmentation in ImageJ was applied to quantify the mitochondrial area from the binarized images.

Cardiac ultrasound imaging and strain analysis

Cardiac function in septic mice was evaluated using a high-resolution ultrasound system (Mindray Animalcare Co., Shenzhen, China). Mice were anesthetized with 1.5% isoflurane in oxygen and positioned on a temperature-controlled imaging platform. Two-dimensional B-mode and M-mode echocardiographic images were acquired from the parasternal long-axis and short-axis views. Left ventricular end-diastolic internal diameter (LVIDd) and end-systolic internal diameter (LVIDs) were measured from M-mode traces. Fractional shortening (FS) was calculated as (LVIDd − LVIDs)/LVIDd × 100%, and ejection fraction (EF) was derived using the Teichholz formula. Speckle-tracking echocardiography was applied to track endocardial and epicardial motion, and left ventricular anterior wall strain was analyzed to assess regional myocardial function. Ultrasound transmission gel was used to ensure optimal acoustic coupling. Following imaging, mice were maintained on a 37 °C warming pad until full recovery from anesthesia.

Statistical analysis

All of these results were expressed as means ± SD. The data were presented in bar charts, and the statistical inference was made by using Student's *t*-test or Mann–Whitney test. Data testing for differences among multiple means was compared by one-way ANOVA. $P < 0.05$ was considered to be statistically significant. All statistical analyses were performed using GraphPad Prism software, version 9.0.

Reagents and sources

Detailed information on the reagents and sources used in this study is provided in Supplementary Table 2.

Data availability

Source data are provided with this paper.

References

1. Kim, H. et al. Cleavage-responsive biofactory T cells suppress infectious diseases-associated hypercytokinemia. *Adv. Sci. (Weinh.)* **9**, e2201883 (2022).
2. Wang, D. et al. Protection of zero-valent iron nanoparticles against sepsis and septic heart failure. *J. Nanobiotechnology* **20**, 405 (2022).
3. Baghdadi, J. D. et al. Association of a care bundle for early sepsis management with mortality among patients with hospital-onset or community-onset sepsis. *JAMA Intern. Med.* **180**, 707–716 (2020).
4. Ouyang, M. et al. Heart-targeted amelioration of sepsis-induced myocardial dysfunction by microenvironment responsive nitric oxide nanogenerators in situ. *J. Nanobiotechnology* **20**, 263 (2022).
5. Chen, L. et al. Nanotherapies for sepsis by regulating inflammatory signals and reactive oxygen and nitrogen species: new insight for treating COVID-19. *Redox Biol.* **45**, 102046 (2021).
6. Gutmann, C. et al. SARS-CoV-2 RNAemia and proteomic trajectories inform prognostication in COVID-19 patients admitted to intensive care. *Nat. Commun.* **12**, 3406 (2021).
7. Hao, S. et al. Identification and validation of a novel mitochondrion-related gene signature for diagnosis and immune infiltration in sepsis. *Front Immunol.* **14**, 1196306 (2023).
8. Perales-Clemente, E. et al. Allotopic expression of mitochondrial-encoded genes in mammals: achieved goal, undemonstrated mechanism or impossible task? *Nucleic Acids Res.* **39**, 225–234 (2011).
9. Cao, Y. et al. Miro2 regulates inter-mitochondrial communication in the heart and protects against TAC-induced cardiac dysfunction. *Circ. Res.* **125**, 728–743 (2019).
10. Nakhle, J., Rodriguez, A. M. & Vignais, M. L. Multifaceted roles of mitochondrial components and metabolites in metabolic diseases and cancer. *Int J. Mol. Sci.* **21**, 12 (2020).
11. Wu, M. et al. TRIM72 alleviates muscle inflammation in mdx mice via promoting mitophagy-mediated NLRP3 inflammasome inactivation. *Oxid. Med. Cell Longev.* **2023**, 8408574 (2023).
12. Su, Y. A. et al. Rat mitochondrion-neuron focused microarray (rMNChip) and bioinformatics tools for rapid identification of differential pathways in brain tissues. *Int. J. Biol. Sci.* **7**, 308–322 (2011).
13. Shao, L. W. et al. Histone deacetylase HDA-1 modulates mitochondrial stress response and longevity. *Nat. Commun.* **11**, 4639 (2020).
14. Wei, Q. et al. MicroRNA-668 represses MTP18 to preserve mitochondrial dynamics in ischemic acute kidney injury. *J. Clin. Invest* **128**, 5448–5464 (2018).
15. Bramkamp, M. Bacterial dynamin-like proteins reveal mechanism for membrane fusion. *Nat. Commun.* **9**, 3993 (2018).
16. Zeng, X. et al. Activated Drp1 regulates p62-mediated autophagic flux and aggravates inflammation in cerebral ischemia-reperfusion via the ROS-RIP1/RIP3-exosome axis. *Mil. Med. Res.* **9**, 25 (2022).
17. Wu, Y. et al. Molecular mechanisms of autophagy and implications in liver diseases. *Liver Res.* **7**, 56–70 (2023).
18. Le, T. V., Truong, N. H. & Holterman, A. X. L. Autophagy modulates physiologic and adaptive response in the liver. *Liver Res.* **7**, 304–320 (2023).
19. Bowes, T. & Gupta, R. S. Novel mitochondrial extensions provide evidence for a link between microtubule-directed movement and mitochondrial fission. *Biochem. Biophys. Res. Commun.* **376**, 40–45 (2008).
20. Huang, X. et al. Kissing and nanotunneling mediate inter-mitochondrial communication in the heart. *Proc. Natl. Acad. Sci. USA* **110**, 2846–2851 (2013).
21. Vincent, A. E. et al. Mitochondrial nanotunnels. *Trends Cell Biol.* **27**, 787–799 (2017).
22. Sobrano Fais, R. et al. NLRP3 activation contributes to endothelin-1-induced erectile dysfunction. *J. Cell Mol. Med.* **27**, 1–14 (2023).
23. Irazoki, A. et al. Coordination of mitochondrial and lysosomal homeostasis mitigates inflammation and muscle atrophy during aging. *Aging Cell* **21**, e13583 (2022).
24. Dong, M. Q. et al. Leukocyte cell-derived chemotaxin 2 (LECT2) regulates liver ischemia-reperfusion injury. *Liver Res.* **8**, 165–171 (2024).
25. Eisner, V. et al. Mitochondrial fusion dynamics is robust in the heart and depends on calcium oscillations and contractile activity. *Proc. Natl. Acad. Sci. USA.* **114**, E859–E868 (2017).
26. Qin, J. et al. ER-mitochondria contacts promote mtDNA nucleoids active transportation via mitochondrial dynamic tubulation. *Nat. Commun.* **11**, 4471 (2020).
27. Wang, C. et al. Dynamic tubulation of mitochondria drives mitochondrial network formation. *Cell Res.* **25**, 1108–1120 (2015).
28. Vincent, A. E. et al. The spectrum of mitochondrial ultrastructural defects in mitochondrial myopathy. *Sci. Rep.* **6**, 30610 (2016).
29. Picard, M. & Shirihai, O. S. Mitochondrial signal transduction. *Cell Metab.* **34**, 1620–1653 (2022).
30. Wallace, P. J. et al. The effects of sulfhydryl inhibitors and cytochalasin on the cytoplasmic and cytoskeletal actin of human neutrophils. *J. Cell Physiol.* **132**, 325–330 (1987).
31. McArthur, K. et al. BAK/BAX macropores facilitate mitochondrial herniation and mtDNA efflux during apoptosis. *Science.* **359**, eaao6047 (2018).
32. Song, Z. et al. Inhibition of Drp1- Fis1 interaction alleviates aberrant mitochondrial fragmentation and acute kidney injury. *Cell Mol. Biol. Lett.* **29**, 31 (2024).

33. Duan, C. et al. Activated Drp1 initiates the formation of endoplasmic reticulum-mitochondrial contacts via Shrm4-mediated actin bundling. *Adv. Sci. (Weinh.)* **10**, e2304885 (2023).
34. Korobova, F., Ramabhadran, V. & Higgs, H. N. An actin-dependent step in mitochondrial fission mediated by the ER-associated formin INF2. *Science* **339**, 464–467 (2013).
35. Hong, W. et al. From symbiosis to immunity: the evolutionary revival of mitochondrial defense programs in inflammatory diseases. *Cell. Commun. Signal* **24**, 219 (2026).
36. Ramirez-Weber, F. A. & Kornberg, T. B. Cytonemes: cellular processes that project to the principal signaling center in Drosophila imaginal discs. *Cell* **97**, 599–607 (1999).
37. Rustom, A. et al. Nanotubular highways for intercellular organelle transport. *Science* **303**, 1007–1010 (2004).
38. Kim, J., Kim, H. S. & Chung, J. H. Molecular mechanisms of mitochondrial DNA release and activation of the cGAS-STING pathway. *Exp. Mol. Med.* **55**, 510–519 (2023).
39. Haileselassie, B. et al. Drp1/Fis1 interaction mediates mitochondrial dysfunction in septic cardiomyopathy. *J. Mol. Cell Cardiol.* **130**, 160–169 (2019).
40. Murphy, M. P. & O'Neill, L. A. J. A break in mitochondrial endosymbiosis as a basis for inflammatory diseases. *Nature* **626**, 271–279 (2024).
41. Xu, L. & Wang, H. A dual role of inflammation in acetaminophen-induced liver injury. *Liver Res.* **7**, 9–15 (2023).
42. Hong, W. L. et al. Targeting mitochondrial quality control: new therapeutic strategies for major diseases. *Mil. Med. Res.* **11**, 59 (2024).
43. Basu, H. et al. FHL2 anchors mitochondria to actin and adapts mitochondrial dynamics to glucose supply. *J. Cell Biol.* **220**, e201912077 (2021).
44. Habibe, J. J., Clemente-Olivo, M. P. & de Vries, C. J. How (epi)genetic regulation of the LIM-domain protein FHL2 impacts multifactorial disease. *Cells* **10**, 2611 (2021).
45. Liang, Y. et al. Four and a half LIM domain protein signaling and cardiomyopathy. *Biophys. Rev.* **10**, 1073–1085 (2018).
46. Zaninello, M. & Bean, C. Highly specialized mechanisms for mitochondrial transport in neurons: from intracellular mobility to intercellular transfer of mitochondria. *Biomolecules* **13**, 938 (2023).
47. Liu, X. et al. Force-induced tail-autotomy mitochondrial fission and biogenesis of matrix-excluded mitochondrial-derived vesicles for quality control. *Proc. Natl. Acad. Sci. USA.* **121**, e2217019121 (2024).
48. Khosravi, S. & Harner, M. E. The MICOS complex, a structural element of mitochondria with versatile functions. *Biol. Chem.* **401**, 765–778 (2020).
49. Ren, W. et al. Visualization of cristae and mtDNA interactions via STED nanoscopy using a low saturation power probe. *Light Sci. Appl.* **13**, 116 (2024).
50. Duan, C. et al. Mitochondrial Drp1 recognizes and induces excessive mPTP opening after hypoxia through BAX-PiC and LRRK2-HK2. *Cell Death Dis.* **12**, 1050 (2021).
51. Liu, Z. et al. XBP1 deficiency promotes hepatocyte pyroptosis by impairing mitophagy to activate mtDNA-cGAS-STING signaling in macrophages during acute liver injury. *Redox Biol.* **52**, 102305 (2022).
52. Cecconi, M. et al. Sepsis and septic shock. *Lancet* **392**, 75–87 (2018).
53. Liu, B. H. et al. Mitochondrial quality control in human health and disease. *Mil. Med. Res.* **11**, 32 (2024).
54. Zhang, Q. et al. Circulating mitochondrial DAMPs cause inflammatory responses to injury. *Nature* **464**, 104–107 (2010).
55. Fung, T. S., Chakrabarti, R. & Higgs, H. N. The multiple links between actin and mitochondria. *Nat. Rev. Mol. Cell Biol.* **24**, 651–667 (2023).
56. Liu, R. et al. Low-dose Olaparib improves septic cardiac function by reducing ferroptosis via accelerated mitophagy flux. *Pharm. Res.* **200**, 107056 (2024).
57. Victorelli, S. et al. Apoptotic stress causes mtDNA release during senescence and drives the SASP. *Nature* **622**, 627–636 (2023).
58. Wen, L. et al. Targeted inhibition of NEK7 preventing sepsis-induced cardiomyopathy by inhibiting NLRP3 inflammasome. *Int. Immunopharmacol.* **151**, 114245 (2025).
59. Hong, W. et al. FXR/ASS1 axis attenuates the TAA-induced liver injury through arginine metabolism. *Biochem. Biophys. Res. Commun.* **611**, 31–37 (2022).

Acknowledgements

The work of Multi-SIM and STORM were supported by the Nanoinsights (https://www.naxi-tech.com). The work of HIS-SIM was supported by CSR-Biotech (https://www.csr-biotech.com).

Author contributions

D.C.Y. and H.W.L wrote the manuscript. H.W.L., L.S.Y. and R.S. were responsible for most of the cellular experiments. S.R. and R.X.P. were responsible for most of the animal experiments. W.J.F., L.Y.F. and C.Q. were responsible for searching, sorting, and summarizing the references. H.W.L. and L.X.F were responsible for plasmid construction. D.C.Y., M.R.Y. and H.H. were responsible for the funding of this study. L.L.M., Z.Z.C., M.D.Q. and J.C. were responsible for the manuscript editing and revising. All authors have read and approved the final version of the manuscript.

Funding

This work was supported by the National Natural Science Foundation of China (Nos. 82472182 and 82272252), the General Project of the Chongqing Natural Science Foundation (CSTB2023NSCQ-MSX0192 and CSTB2023NSCQ-ZDJ0016) and Chongqing National Talent Reserve Project (HBRC202419). All these from D.C.Y.

Competing interests

The authors declare no competing interests.

Additional information

Supplementary information The online version contains supplementary material available at https://doi.org/10.1038/s41467-026-73523-0.

Correspondence and requests for materials should be addressed to João. Conde, Liangming Liu or Chenyang Duan.

Peer review information *Nature Communications* thanks Xiaohui Wang, Mingui Fu, and the other, anonymous, reviewer(s) for their contribution to the peer review of this work. A peer review file is available.

Inclusion & Ethics All animal experiments were conducted in compliance with relevant guidelines and regulations and were approved by the Institutional Animal Care and Use Committee of the Second Affiliated Hospital of Chongqing Medical University [Approval No. 2022 (222)]. This study was performed in accordance with the ARRIVE 2.0 guidelines. It is noteworthy that this research did not involve any human participants or stem cell studies. Animal sex and other characteristics that may influence experimental outcomes are described in the methods section. Details of housing and husbandry are provided where relevant.

[1]Department of Critical Care Medicine, The Second Affiliated Hospital of Chongqing Medical University, Chongqing, China. [2]Department of Cardiovascular Surgery, Xinqiao Hospital, Army Medical University, Chongqing, China. [3]Perioperative and System Medicine Laboratory and Department of Anaesthesiology, Children's Hospital, Zhejiang University School of Medicine, National Clinical Research Center for Children and Adolescents' Health and Diseases, Hangzhou, China. [4]Division of Anaesthetics, Pain Medicine and Intensive Care, Department of Surgery and Cancer, Faculty of Medicine, Imperial College London, Chelsea & Westminster Hospital, London, UK. [5]Department of Critical Care Medicine, The Second Affiliated Hospital, Zhejiang University School of Medicine, Hangzhou, China. [6]Department of Radiation Oncology and Shandong Provincial Key Laboratory of Radiation Oncology, Shandong Cancer Hospital and Institute, Shandong First Medical University and Shandong Academy of Medical Sciences, Jinan, China. [7]State Key Laboratory of Trauma and Chemical Poisoning, Department of Shock and Transfusion, Daping Hospital, Army Medical University, Chongqing, China. [8]Chongqing Institute of Collaborative Science and Technology Innovation, Chongqing, China. [9]Present address: Comprehensive Health Research Centre (CHRC), NOVA Medical School, Faculdade de Ciências Médicas, NMS | FCM, Universidade NOVA de Lisboa, Lisboa, Portugal. [10]These authors contributed equally: Weilong Hong, Ruiyan Ma, Shiyun Long, Rui Song. ✉e-mail: joao.conde@nms.unl.pt; lmliu62@tmmu.edu.cn; duanchenyang1991@cqmu.edu.cn